Hillslope permeability architecture controls on subsurface transit time distribution and flow paths

A.A. Ameli [a,d,*], N. Amvrosiadi [b], T. Grabs [b], H. Laudon [c], I.F. Creed [a], J.J. McDonnell [d,e], K. Bishop [b,f]

[a] Department of Biology, Western University, London, Ontario, Canada
[b] Department of Earth Sciences, Air Water and Landscape Sciences, Uppsala University, Uppsala, Sweden
[c] Department of Forest Ecology and Management, Swedish University of Agricultural Sciences, Umeå, Sweden
[d] Global Institute for Water Security, School of Environment and Sustainability, University of Saskatchewan, Saskatoon, Saskatchewan, Canada
[e] School of Geosciences, University of Aberdeen, Aberdeen, UK
[f] Department of Aquatic Sciences and Assessment, Swedish University of Agricultural Sciences, Uppsala, Sweden

ARTICLE INFO

SUMMARY

Defining the catchment transit time distribution remains a challenge. Here, we used a new semi-analytical physically-based integrated subsurface flow and advective–dispersive particle movement model to assess the subsurface controls on subsurface water flow paths and transit time distributions. First, we tested the efficacy of the new model for simulation of the observed groundwater dynamics at the well-studied S-transect hillslope (Västrabäcken sub-catchment, Sweden). This system, like many others, is characterized by exponential decline in saturated hydraulic conductivity and porosity with soil depth. The model performed well relative to a tracer-based estimate of transit time distribution as well as observed groundwater depth–discharge relationship within 30 m of the stream. Second, we used the model to assess the effect of changes in the subsurface permeability architecture on flow pathlines and transit time distribution in a set of virtual experiments. Vertical patterns of saturated hydraulic conductivity and porosity with soil depth significantly influenced hillslope transit time distribution. Increasing infiltration rates significantly decreased mean groundwater age, but not the distribution of transit times relative to mean groundwater age. The location of hillslope hydrologic boundaries, including the groundwater divide and no-flow boundary underlying the hillslope, changed the transit time distribution less markedly. These results can guide future decisions on the degree of complexity that is warranted in a physically-based rainfall–runoff model to efficiently and explicitly estimate time invariant subsurface pathlines and transit time distribution.

© 2016 Elsevier B.V. All rights reserved.

1. Introduction

The transit time distribution (TTD) and water flow pathlines are fundamental descriptions of a catchment (McDonnell and Beven, 2014). The TTD (also referred to as the probability density function of transit times) describes how hillslopes store, mix and release water and solutes. The flow pathlines define the different sequences of subsurface environments traversed by water entering the catchment at different points and at different times. The subsurface TTD and flow pathlines structure are important for both the quantity and quality of stream flow (Birkel et al., 2011;

Vaché and McDonnell, 2006). This combination of information is valuable for constraining where and for how long biogeochemical processes can occur in the riparian zone; for analyzing how the movement of water alters the critical zone itself, and for understanding how different sources of water combine to yield the dynamics of runoff chemistry (Pinay et al., 2015). For example, knowledge of subsurface TTD and flow pathlines can, in the case of mercury contamination, help identify biogeochemical processes that are more or less likely to play an important role due to the amount of time spent in a particular soil zone relative to when that water reaches the stream (Eklöf et al., 2014). Due to the complexity of unravelling catchment TTD, few runoff generation or water quality models explicitly include such representations.

Improved understanding of controls on flow pathlines and TTD is a challenge facing hydrologists. An important step forward is the exploration of how key features of catchment structure, including permeability architecture (defined here as the vertical distribution

---

* Corresponding author at: Department of Biology, Biological & Geological Sciences Building, Western University, London, Ontario N6A 5B7, Canada. Tel.: +1 6474708182.

E-mail address: aameli2@uwo.ca (A.A. Ameli).

of hydraulic conductivity and porosity throughout the catchment control volume) and the locations of hydrological boundaries will influence the TTD and flow paths (Basu et al., 2012). Most methods currently used to define TTD do not explicitly take into account subsurface flow physics and flow pathlines, or even basic groundwater flow theory controlling subsurface flow movement. Conceptual convolution method (e.g., Hrachowitz et al., 2009, 2010; Kirchner et al., 2000) and storage selection scheme (Botter, 2012; Botter et al., 2011; Harman, 2015; Klaus et al., 2015; Rinaldo et al., 2015, 2011), are based mainly on the assessment of precipitation and stream flow tracer data without explicit characterization of the subsurface permeability architecture. Indeed, these approaches often use the tracer data to compute the best fit parameters of an *a priori* assumed distribution of transit times for a conceptual convolution scheme, or to calibrate storage-related parameters of *a priori* defined storage functions that are assumed to control the type of water mixing and release for the storage selection scheme. Ali et al. (2014), Basu et al. (2012) and more recently Kirchner (2016) have commented on the limitations of these implicit schemes for the prediction of TTD. They (and others) have noted that these models are difficult to analyze in relation to subsurface physical heterogeneity which can impact the variability in hillslope flow pathline and hence the corresponding TTDs (Ali et al., 2014; Birkel et al., 2011; Fiori and Russo, 2008; Hrachowitz et al., 2009, 2010).

Useful simulations of mean transit time (MTT) and TTD through an integrated subsurface flow and transport simulation have been done using numerical approaches (e.g., Ali et al., 2014; Basu et al., 2012; Cardenas and Jiang, 2010; Fiori and Russo, 2008; Kollet and Maxwell, 2008; Molénat et al., 2013; Sayama and McDonnell, 2009). Numerical approaches were also used to directly model groundwater age through solving novel groundwater age governing equations (Goode, 1996; Woolfenden and Ginn, 2009). And, more recent work has explored the effect of climate on TTD of groundwater more broadly (Maxwell et al., 2015). These physically-based models are able to take into account the basic groundwater flow and transport theories. Numerical approaches were also used to assess the impact of subsurface vertical and lateral heterogeneity on TTD. Kollet and Maxwell (2008) coupled the ParFlow numerical steady-state model with a Lagrangian particle tracking approach to assess the impact of changes in macro-dispersion values on TTD. Cardenas and Jiang (2010) linked a topography-driven steady-state flow model within the numerical COMSOL platform with an Advection–Dispersion–Diffusion transport equation to assess the impact of the rate of exponential decline in saturated hydraulic conductivity (K_s) with depth on TTD. Fiori and Russo (2008) and Fiori et al. (2009) also developed 3-D numerical flow and transport models to assess the impact of statistically-driven heterogeneity in saturated hydraulic conductivity on the shape of TTD.

These numerical modeling approaches, however, considered relatively smooth changes in subsurface material properties both laterally and vertically. For example, Fiori and Russo (2008) clearly explained that the level of subsurface heterogeneity that they considered in their numerical experiment was "moderate" compared to the much stronger heterogeneity that can be found in many catchments. Cardenas and Jiang (2010) also considered gradual changes in K_s with depth; the largest rate of exponential decline in K_s with soil depth they considered was $\alpha = 0.01$. But much more rapid changes in K_s with depth are typical in forested catchments (e.g., Harr, 1977; McGuire and McDonnell, 2010), especially in glacial tills soils where exponential change values of α up to 4 are more typical (e.g., Grip, 2015; Lundin, 1982; Nyberg, 1995; Seibert et al., 2011). Ali et al. (2014) noted the lack of characterization of large scale spatial heterogeneity as one of the major limitations of numerical methods which may impact the verisimilitude

of flow paths and transit times simulated using these approaches. A systematic assessment of how rapid (exponential) changes in the permeability architecture influence TTD and flow pathlines pose particular considerations for grid-based numerical approaches since many discrete sub-layers are needed to represent the rapid changes in K_s and porosity values. This treatment of vertical heterogeneity in permeability architecture can compromise the efficiency of grid-based numerical flow and transport schemes when systematically testing hypotheses about how interactions among different depth functions for K_s and porosity influence hillslope TTD and flow pathlines.

Recently, Ameli et al. (2013) and Ameli and Craig (2014) developed a new "grid-free" integrated flow and transport scheme for explicit simulation of 2-D and 3-D time-invariant subsurface flow pathlines through unconfined aquifers, and transit times along those pathlines. The coupled saturated–unsaturated semi-analytical solutions satisfy exactly the saturated and unsaturated governing equations (including mass balance). The semi-analytical solutions also take into account infiltration rate, natural geometry of the unconfined aquifer and calculate the *a priori* unknown locations of water table and seepage faces using a free boundary condition rather than assuming the water table as a replica of the ground surface (i.e. the topography-driven water table assumption). Without the need for implementation of vertical discretization (i.e. sub-layers), these grid-free approaches more recently have been extended to account explicitly and exactly for various rates of exponential decline in saturated hydraulic conductivity with soil depth (Ameli et al., 2016); a characteristic feature of many till-mantled "critical zone" environments. This steady-state scheme provides a continuous map of head and velocity in the entire hillslope without the need for interpolation, efficiently generating subsurface flow pathlines toward a stream and transit times along these pathlines. Thus this approach allows for an explicit and systematic exploration of the effects of subsurface vertical heterogeneity, hydrological boundaries and infiltration rate on "time invariant" TTD and flow pathlines in a 2-D hillslope.

Here we provide the first field test of this semi-analytical model against the observed hillslope flow and transport dynamics in an extensively studied till-mantled hillslope in the Västrabäcken sub-catchment of the Krycklan Basin (Laudon et al., 2013). We then use this physically based model as the test bed for virtual experiments that systematically explore the impacts of changing physical features and permeability architecture of the hillslope and infiltration rate on the transit time distribution and flow pathlines. Specifically we:

(1) Assess the performance of the semi-analytical approach presented by Ameli et al. (2016) in simulating internal hydrometric observations along the hillslope and isotopic observations at the catchment.
(2) Use virtual experiments to explore the influence of changing subsurface conditions (saturated hydraulic conductivity and porosity change with soil depth, mechanical dispersion, location of no-flow boundary underlying the hillslope, hillslope length and infiltration rate) on subsurface TTD, mean groundwater age and water flow pathlines.

2. Material and methods

2.1. Hillslope description

The S-transect hillslope is located on the 12 ha Västrabäcken sub-catchment (denoted C2 in the Krycklan Basin, Fig. 1a–c), which is part of the Svartberget catchment (Laudon et al., 2013). The sub-catchment topography is characterized by gentle slopes, and the subsurface consists of well-developed podzols, overlying glacial
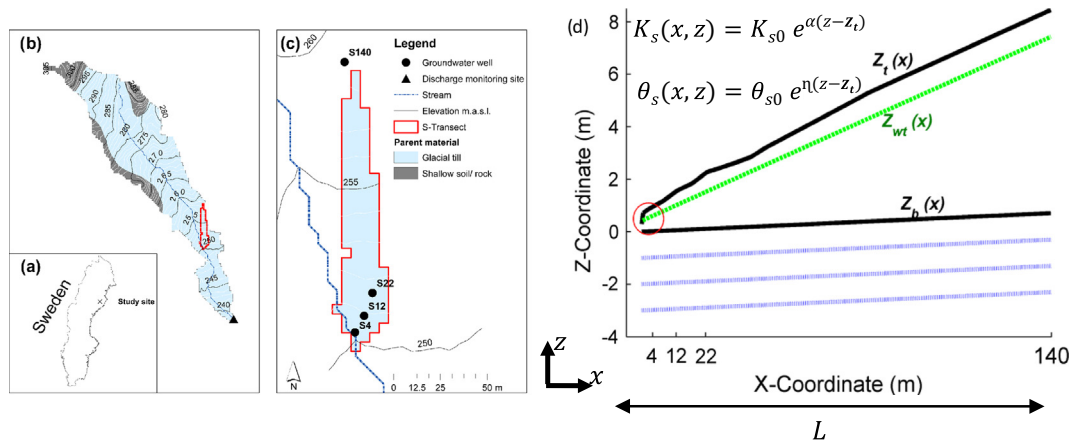
Fig. 1. Layout of the S-transect. (a) Study location, (b) plan view of 12 ha Västrabäcken sub-catchment and (c) plan view of the S-transect along with the location of discharge measurement site and groundwater measurement wells. Groundwater wells, referred to as S4, S12, S22 and S140, located at 4, 12, 22 and 140 m (sub-catchment divide) from the stream. (d) 2-D cross section of the S-transect used here with a length of L. The topographic surface $Z_t(x)$ was generated from the original 5 m LIDAR DEM. Saturated hydraulic conductivity (K_s) and porosity (θ_s) decay exponentially with depth. α and η are the parameters of the exponential relationship between saturated hydraulic conductivity and porosity with depth, respectively. K_{s0} [L T^{-1}] and θ_{s0} are the saturated hydraulic conductivity and porosity along the topographic surface ($z_t(x)$). The topographic surface ($z_t(x)$) is subject to a Dirichlet condition along the surface water course (red circle) with a constant head of 0.45 m, and specified infiltration function ($R(x)$) along the remaining part. The bottom boundary $z_b(x)$ with a slope of 0.5% and divide (right side of the hillslope at $X = 140$ m) are assumed impermeable. The a priori unknown water table $z_{WT}(x)$ is also calculated as a boundary with zero pressure head (green line). The blue lines show the alternative locations of the no-flow boundary underlying the hillslope used in the Section 3.7. (For interpretation of the references to color in this figure legend, the reader is referred to the web version of this article.)

till. This hillslope has been the subject of a large number of previous hydrological (Laudon et al., 2004; Peralta-Tapia et al., 2014; Stähli et al., 2001) and biogeochemical (Bishop et al., 1995; Cory et al., 2007; Klaminder et al., 2006; Leith et al., 2014; Peralta-Tapia et al., 2016; Seibert et al., 2009) studies. The sub-catchment vegetation is dominated by Norway Spruce and Scots Pine with an undercover of bilberry. Average daily precipitation and actual evapotranspiration during the study period (13.10.2013–22.09.2014) were 1.79 and 0.96 mm/day, respectively, where daily actual evapotranspiration was calculated using the HBV model (Seibert, 2000). Precipitation during the study period was 653 mm, slightly higher than the long-term (1990–2012) mean annual precipitation (630 mm). Temperature during the study period was 4.4 °C, higher than the long-term (1990–2012) mean annual temperature (2.2 °C). Therefore, the study period was slightly wetter and warmer than the average conditions of the 23 previous years.

Daily stream discharge was taken from the continuous measurements at a V-notch weir located 0.5 km downstream of the S-transect (Fig. 1a). During the study period, the 10th percentile, median, average, and 90th percentile daily discharge were 0.12, 0.50, 0.80 and 1.80 mm/d, respectively, which were consistent with long term daily stream discharge. Average daily groundwater depth measurements were collected with pressure transducers at four groundwater wells located along the hillslope transect (as defined by the topographic fall line) at 4 m, 12 m, 22 m, and 140 m (sub-catchment divide) from the stream. Sites below these wells were referred to as S4, S12, S22, and S140. Statistical t-tests showed that groundwater depth was significantly related to stream discharge ($p < 0.001$) (Fig. 2, black lines represent the best fit to the observed groundwater depth–discharge relationship). These stream-discharge relationships were used to parameterize the subsurface flow model in this paper. Soil samples were collected from different depths at S4, S12, S22, and the water content was measured at different matric tensions in order to calculate soil moisture retention curves (Nyberg et al., 2001). The unsaturated Gardner model (Gardner, 1958), used here to characterize the vadose zone behavior, was fitted to the observed soil moisture

retention data which estimated the Gardner sorptive number as $\beta = 1$ 1/m and an air entry pressure of $\varphi^e = 0.05$ m. The water content at zero matric tension was used as the porosity (θ_s) at each depth. The best exponential fit function to the porosity–depth measurements of the mineral soil was $\theta_s(x, z) = 0.49 e^{0.26(z-z_t)}$, where ($z - z_t$) refers to the soil depth. The K_s-depth relationship was also measured in the sub-catchment using the permeameter method (Bishop, 1991). The best fit exponential function to the observed K_s-depth data was $k_s(x, z) = 86 e^{2.46(z-z_t)}$ m/d.

Peralta-Tapia et al. (2016) analyzed a 10-year time series isotopic data (δ^{18}O and δ^2H) for stream and precipitation waters within the Svartberget catchment to estimate TTD using a convolution approach; the stream data was collected from the same stream as S-transect discharged into. A Gamma distribution with a shape parameter of 0.59 was the best fit to their observed isotopic data (black line in Fig. 2b). In addition, in an analysis of soil water δ^{18}O during snowmelt/spring flood on the S-transect, Laudon et al. (2004) showed that the infiltrating rainfall/snowmelt does not penetrate deeper than 90 cm at S22 before and after spring flood. These findings were also used here to assess the efficacy of the subsurface flow and transport model in simulating the TTD and flow pathlines.

A 5-m LiDAR Digital elevation model (DEM) was used to derive sub-catchment divides and to create a 2-D representation of the surface of the S-transect along the topographic fall line (Fig. 1d). The S-transect is characterized by a planar geometry with an almost uniform width and slope. The ratio of hillslope width variation with respect to the hillslope length was almost 0.03 and the slope of the hillslope in the direction perpendicular to the slope varied in a range of less than 2%. The terrain analysis of the DEM also suggested that the flow direction in the transect is North–South. Thus, we believe that the 2-D representation should be an appropriate emulation of the natural subsurface behavior within the S-transect. Groundwater well locations (Fig. 1c) were then projected onto this 2-D representation; observations showed there was no net recharge lower than 30 cm below the streambed and so we placed the no-flow boundary at this depth (Fig. 1d).
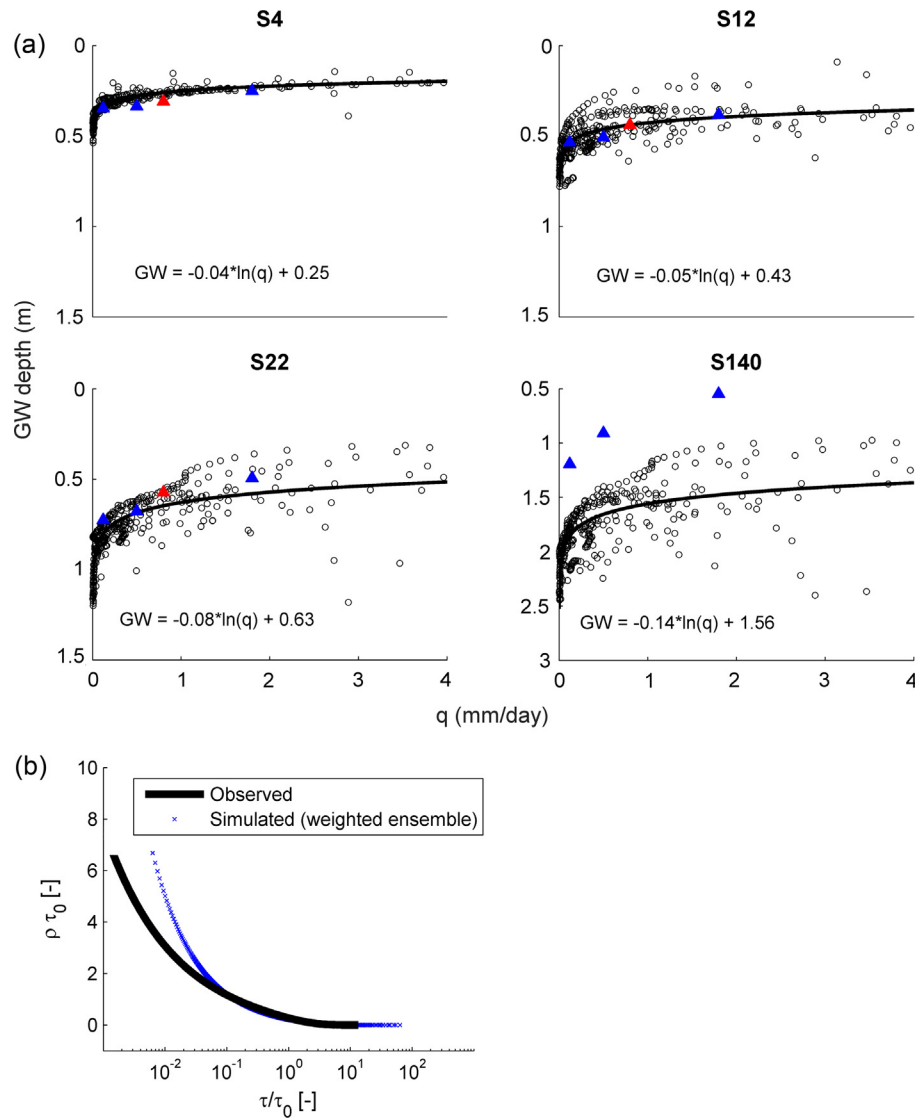
Fig. 2. Comparison between observed and simulated hydrological and transport processes. (a) Observed (circles) and simulated (triangles) relationship between groundwater depth and specific discharge at sections S4, S12, S22 and S140. The black lines represent the best fit to the observed groundwater depth–discharge relationship based on data collected from October 2013 to October 2014. Red and blue triangles represent the simulated relationship between groundwater depth and discharge in the calibration (red) and validation (blue). (b) Observed and simulated (weighted ensemble) dimensionless TTD. The former was obtained by imposing a convolution approach on the 10-year time series of isotopic data (δ^{18}O and δ^2H) for stream water and precipitation within the Svartberget catchment of which the S-transect and the Västrabäcken sub-catchment are a part; the stream data was collected from the same stream as S-transect discharged into. The simulated weighted ensemble TTD was calculated by assembling simulated transit times of water particles discharged into the stream in response to various flow rates. The transit times were weighted based on the frequency of occurrence of the corresponding stream discharge rates in annual discharge frequency distribution. (For interpretation of the references to color in this figure legend, the reader is referred to the web version of this article.)

2.2. Modeling method

The 2D schematic of S-transect hillslope with an exponential decay in saturated hydraulic conductivity and porosity with depth is shown in Fig. 1d. The semi-analytical series solution method of Ameli et al. (2016) was used to calculate the continuous fields of saturated and unsaturated hydraulic head and velocity in the entire hillslope (Appendix A). This solution was coupled with a Random Walk Particle Tracking (RWPT) transport method to generate the flow pathlines and transit time along these pathlines.

2.2.1. Uniform Random Walk Particle Tracking (RWPT) method

The calculated discharge potential function (Eq. (A.1)) and Kirchhoff potential (Eq. (A.2)) in the saturated and unsaturated zones, respectively, can be coupled with a uniform RWPT scheme (e.g., Salamon et al., 2006) to generate flow pathlines from the topographic surface to the surface water course and calculate transit time along the pathlines. To do that, first, continuous maps of Darcy fluxes throughout the entire saturated zone ($q_{sx}(x,z)$ & $q_{sz}(x,z)$) and Darcy–Buckingham fluxes in the unsaturated zone ($q_{ux}(x,z)$ & $q_{uz}(x,z)$) are required. These fluxes can be calculated as:

$$q_{sx}(x,z) = e^{\alpha(z-z_t)}\frac{d\phi_s(x,z)}{dx} \ \& \ q_{sz}(x,z) = e^{\alpha(z-z_t)}\frac{d\phi_s(x,z)}{dz} \tag{1a}$$

$$q_{ux}(x,z) = e^{\alpha(z-z_t)}\frac{d\phi_u(x,z)}{dx} \ \& \ q_{uz}(x,z)$$
$$= e^{\alpha(z-z_t)}\left[\frac{d\phi_u(x,z)}{dz} + \beta\phi_u(x,z)\right] \tag{1b}$$

Substitution of Eqs. (A.1) and (A.2) into Eq. (1) yields:

$$q_{sx}(x,z) = -e^{\alpha(z-z_t)}\sum_{n=1}^{N}\frac{n\pi}{L}\left(A_n\left[\sin\left(\frac{n\pi}{L}x\right)\exp(\gamma_n z)\right] + B_n\left[\sin\left(\frac{n\pi}{L}x\right)\exp(\bar\gamma_n z)\right]\right) \ \& \ q_{sz}(x,z) = e^{\alpha(z-z_t)}\sum_{n=1}^{N}\left(\gamma_n A_n\left[\cos\left(\frac{n\pi}{L}x\right)\exp(\gamma_n z)\right] + \bar\gamma_n B_n\left[\cos\left(\frac{n\pi}{L}x\right)\exp(\bar\gamma_n z)\right]\right)$$
(2a)

$$q_{ux}(x,z) = e^{\alpha(z-z_t)}\sum_{m=1}^{M}\frac{m\pi}{L}\left(C_m\left[\sin\left(\frac{m\pi}{L}x\right)\exp(\pounds_m z)\right]\frac{\pounds_m}{\frac{m\pi}{L}} + D_m\left[\sin\left(\frac{m\pi}{L}x\right)\exp(\bar\pounds_m z)\right]\frac{\pounds_m}{\frac{m\pi}{L}}\right) \ \& \ q_{uz}(x,z) = e^{\alpha(z-z_t)}\sum_{m=1}^{M}\frac{m\pi}{L}\left(C_m\left[\cos\left(\frac{m\pi}{L}x\right)\exp(\pounds_m z)\right] + D_m\left[\cos\left(\frac{m\pi}{L}x\right)\exp(\bar\pounds_m z)\right]\right)$$
(2b)

Continuous fields of pore water velocity are then calculated as:

$$V_{sx}(x,z) = \frac{q_{sx}(x,z)}{\theta_s(x,z)} \ \& \ V_{sz}(x,z) = \frac{q_{sz}(x,z)}{\theta_s(x,z)}$$
(3a)

$$V_{ux}(x,z) = \frac{q_{ux}(x,z)}{\theta_u(x,z)} \ \& \ V_{uz}(x,z) = \frac{q_{uz}(x,z)}{\theta_u(x,z)}$$
(3b)

where the saturated moisture content (θ_s) is equal to the porosity and is obtained as a function of soil depth $\theta_s(x,z) = \theta_{s0}(x,z)e^{\eta(z-Z_t(x))}$. The unsaturated moisture content (θ_u) is also obtained based on both the suction pressure head (φ) and soil depth at each location $(\theta_u(x,z,\varphi) = \theta_{s0}(x,z)e^{\eta(z-Z_t)}e^{(\beta(\varphi-\varphi^e))})$. Using the calculated continuous fields of V_x and V_z (Eq. (3)) in the entire hillslope, the uniform random walk step of a water particle is given by:

$$x_p^k = x_p^{k-1} + V_x\Delta t + \sqrt{2D_L\Delta t}X_L\frac{V_x}{|V|} - \sqrt{2D_T\Delta t}X_T\frac{V_z}{|V|}$$
(4a)

$$z_p^k = z_p^{k-1} + V_z\Delta t + \sqrt{2D_L\Delta t}X_L\frac{V_z}{|V|} - \sqrt{2D_T\Delta t}X_T\frac{V_x}{|V|}$$
(4b)

where $|V| = \sqrt{V_x^2 + V_z^2} \ \& \ D_L = \alpha_L|V| \ \& \ D_T = \alpha_T|V|$

x_p^k and z_p^k are the particle position at the kth time step, D_L and D_T [$L^2 T^{-1}$] are the longitudinal and transverse mechanical dispersion coefficients, respectively, and α_L and α_T [L] refer to longitudinal and transverse dispersivity of the porous medium. X_L and X_T denote random numbers drawn from a normal distribution with zero mean and unit variance for each particle and each time step (Δt). All particles were initially released at evenly-spaced locations along the topographic surface. The optimum number of initially released particles along the topographic surface was first obtained by performing a sensitivity analysis which assesses the impact of the number of particles on MTT and TTD. The pathlines generated and the residence times along these pathlines were then used to calculate the transit times of water particles discharged into the watercourse. We then fitted various distributions including power-law, Weibull and Gamma distributions to the simulated transit times to characterize the transit time probability density function. As expected, the Gamma distribution was the best fit to the simulated transit times for all examples we solved in this paper. The expression for the Gamma distribution probability density function is expressed as a function of the transit time (τ) as:

$$\rho(\tau) = \frac{\left(\frac{a\tau}{\tau_0}\right)^a}{\tau\Gamma(a)}e^{-a\frac{\tau}{\tau_0}}$$
(5)

where a is the Gamma distribution shape parameter and τ_0 is mean transit time. The shape parameter (a) in the gamma distribution describes how much weight is found in the tails of the distribution, versus near the center, and is a measure of the degree of variability of subsurface transit times (Kirchner, 2016). The ratio of the standard deviation to the mean of transit times equals the square root of $1/a$. Thus, as the Gamma shape parameter decreases, the variability in transit times increases with higher proportions of young and old waters (both tails of the TTD) relative to mean transit time (Godsey et al., 2010). To schematize the degree of variability in transit times, the dimensionless transit time distribution ($\rho\left(\frac{\tau}{\tau_0}\right)\tau_0$) with respect to scaled transit time $\left(\frac{\tau}{\tau_0}\right)$ (as has done in Fiori and Russo (2008)) is also shown in this paper.

2.2.2. Virtual experiment

One possible way forward for synthetic work aimed at understanding the controls on hillslope flow and transport processes, together with the potential interaction among controls, is virtual experimentation. Weiler and McDonnell (2004) defined this as experiments driven by a collective field intelligence and performed using robust modeling approaches. Once our semi-analytical series solution model was parameterized and assessed based on the field data, the impact of different controls was assessed by changing the value of the control (all else being equal) without any further calibration. The interaction among controls was also assessed using a similar approach.

This virtual experimentation approach improves our understanding of how different subsurface structures and infiltration rates influence time-invariant TTD. While the list of possible variables is long, some of the more important factors are: (1) the rate of exponential decline in K_s with soil depth (α); (2) the rate of exponential decline in porosity with soil depth (η); (3) mechanical dispersion (α_L); (4) infiltration rate (R); (5) hillslope length, L (i.e., the distance along the hillslope between the stream and the local subcatchment water divide); and (6) the location of the no-flow boundary underlying the hillslope where Z_a refers to the minimum vertical distance between stream bed and the no-flow boundary.

The modeling approach we used here can efficiently take into account systematic vertical changes in K_s and porosity with depth as well as these other aforementioned factors. As will be shown later, the impact of changes in K_s with soil depth (factor 1) on subsurface flow characteristics is significant. Thus, the effects of factors 2–6 were assessed for two end members of exponential decline in saturated hydraulic conductivity with soil depth (i.e. extreme vertical heterogeneity in k_s which is defined in this paper by $\alpha = 3$ and a homogenous k_s with $\alpha = 0$) to incorporate the interaction among these factors. Table 1 reports the list of controlling factors that were varied in the virtual experiments and their tested levels. The selected values of controlling factors used in the virtual experiments were from the range observed in till environments with the exception of zero values for α, η and α_L which represent a pure homogenous media as well as $\eta = 0.75$, which represents extreme heterogeneity in porosity.

3. Results

The efficacy the semi-analytical series solution method of Ameli et al. (2016) in simulating the groundwater depth–discharge relationship at S4, S12, S22, and S140 as well as TTD of water particles discharged into the stream is assessed. The model is then used to

Table 1
List of controlling factors (i.e. permeability, hydrological boundary and flow rate parameters) that were varied in the virtual experiments and their tested levels. Z_a is the minimum vertical distance calculated between stream bed and no-flow boundary at the bottom of the hillslope (Section 3.7). The original and alternative bottom boundaries used in this section are shown in Fig. 1d.

Factor	Parameter								
	k_{s0} [m/d]	α [1/m]	θ_{s0} []	η []	R [mm/d]	α_L [cm]	α_T [cm]	L [m]	z_a [m]
α (Section 3.2)	100	0; 1; 2; 3	0.49	0.26	1.8	1	0.01	140	0.30
η (Section 3.3)	100	0; 3	0.49	0; 0.25; 0.5; 0.75	1.8	1	0.01	140	0.30
R (Section 3.4)	100	0; 3	0.49	0.26	0.12; 0.5; 0.8; 1.8	1	0.01	140	0.30
α_L (Section 3.5)	100	0; 3	0.49	0.26	1.8	0; 0.1; 1; 10	0; 0.001; 0.01; 0.1	140	0.30
L (Section 3.6)	100	0; 3	0.49	0.26	1.8	1	0.01	80; 100; 120; 140	0.30
z_a (Section 3.7)	100	0; 3	0.49	0.26	1.8	1	0.01	140	0.30; 1.30; 2.30, 3.30

examine the sensitivity of the flow pathlines and TTD to the architecture of the hillslope permeability, location of hydrological boundaries, and infiltration rate in sets of virtual experiment.

3.1. Model calibration, construction of the annual TTD and assessment against independent observations

Our series solution model was calibrated to define the K_s profile (i.e. K_{s0} & α) along the S-transect. The calibration objective was to emulate the observed groundwater depth–discharge relationship at groundwater monitoring wells located at S4, S12, S22 for the average annual runoff rate. Since earlier work on such till hillslopes had suggested that a steady state assumption was valid within several tens of meters from the stream, we chose to prioritize the fit of the three groundwater tubes nearest the stream and did not use the groundwater measuring tube located at S140 (sub-catchment divide) in the calibration process. Note that for this steady state model the infiltration and discharge rates were assumed to be identical. Thus the calibration was made using the annual average discharge of 0.8 mm/d as the infiltration rate. Manually calibrated values of the parameters were $K_{s0} = 100$ m/d and $\alpha = 3$ 1/m. The calibrated exponential function for the saturated hydraulic conductivity–depth relationship was consistent with the best fit exponential function fitted to the observed saturated hydraulic conductivity–depth data obtained using the permeameter method (the best fit parameters from Bishop (1991) were $K_{s0} = 86$ m/d and $\alpha = 2.49$ 1/m).

In the calibration phase, the model accurately simulated the groundwater depth–discharge relationship in the hillslope within 30 m of the water course (the red triangles in Fig. 2a) for the calibration condition of a 0.8 mm/d discharge rate. High flow (1.8 mm/d), median flow (0.5 mm/d) and low flow (0.12 mm/d) were used to test the model in the validation phase (the blue triangles in Fig. 2a). The model accurately reproduced the groundwater level within 30 m of the water course for other discharge rates as well, while further away from the watercourse at S140 in the vicinity of the sub-catchment divide the predicted groundwater levels remained about 0.5–1 m higher than the observed values. This was attributed to the fact that in the vicinity of sub-catchment divide, steady state conditions were not expected as shown by manual hydrometric measurements made on a hillslope close to the one examined in this study (Seibert et al. (2003). The calibrated subsurface flow model provided a continuous map of the velocity field in the entire domain at a given infiltration rate. This was used within Random Walk Particle Tracking (RWPT) analysis to generate flow pathlines and transit times for any given infiltration rate and the associated stream discharge. The optimum number of particles at which MTT and Gamma shape parameter of the fitted TTD converged was 560 (i.e., at each 25 cm interval along the topographic surface) (Table 2). This initial condition was used in the original model and the virtual experiments.

Table 2
Convergence of MTT (Gamma shape parameter) using various numbers of particles initially released from the topographic surface for the calibrated model with $\alpha = 3$ and hypothetical model with $\alpha = 0$. For this convergence analysis $k_{s0} = 100$ [m/d], $\theta_{s0} = 0.49$, $\eta = 0.26$, $R = 1.8$ [mm/d], $\alpha_L = 1$ [cm], $\alpha_T = 0.01$ [cm], $L = 140$ m and $z_a = 0.30$ [m] were considered.

	$N_p = 70$	$N_p = 140$	$N_p = 280$	$N_p = 560$
$\alpha = 3$	145 (0.62)	174 (0.54)	195 (0.52)	199 (0.55)
$\alpha = 0$	64 (0.94)	65 (0.93)	65 (0.93)	65 (0.93)

To compare the model TTD to a tracer-based estimate of TTD, we assumed the catchment flow system to be a succession of steady states. The semi-analytical model TTD was calculated by assembling simulated transit times of water particles discharged into the stream in response to various infiltration rates. These aggregated transit times were weighted according to the frequency of occurrence of the corresponding stream discharge rates (which is here equal to infiltration) in the annual discharge frequency distribution. A Gamma distribution with a shape parameter of 0.51 was the best fit to the simulated ensemble transit times (Fig. 2b) at the S-transect. To simulate transit times, in addition to the calibrated parameters, observed porosity patterns with $\eta = 0.26$, $\theta_{s0} = 0.49$ within the hillslope, as well as longitudinal and transverse dispersivities of 1 cm and 0.01 cm were considered. The dispersivity values spanned what is typical in till environments. The annual ensemble TTD using the calibrated semi-analytical model yielded a Gamma shape parameter of 0.51. This was comparable to the TTD obtained by imposing a convolution approach on the 10-year time series of isotopic data (δ^{18}O and δ^2H) for precipitation and stream runoff from the catchment which yielded a Gamma shape parameter of 0.59 (Fig. 2b). As stated earlier the discharge frequency distribution during the study period was similar to the long term discharge frequency distribution. This, together with the fact that the collected isotopic data was taken from the stream that the S-transect discharged into, suggests that the integrated flow and transport model can reasonably emulate the transport behavior of the hillslope.

3.2. Effect of rate of exponential decline in saturated hydraulic conductivity with soil depth

The model was then used to explore the impact of changing the rate of exponential decline in K_s with soil depth on the distributions of flow pathlines and transit time. As the rate of exponential decline in k_s with depth (α) increases, shallow and deep subsurface flow circulation enhances and lessens, respectively (Fig. 3). This can be tied to the fact that the water table reaches the superficial portion of the hillslope with a relatively higher conductivity closer to the topographic surface.
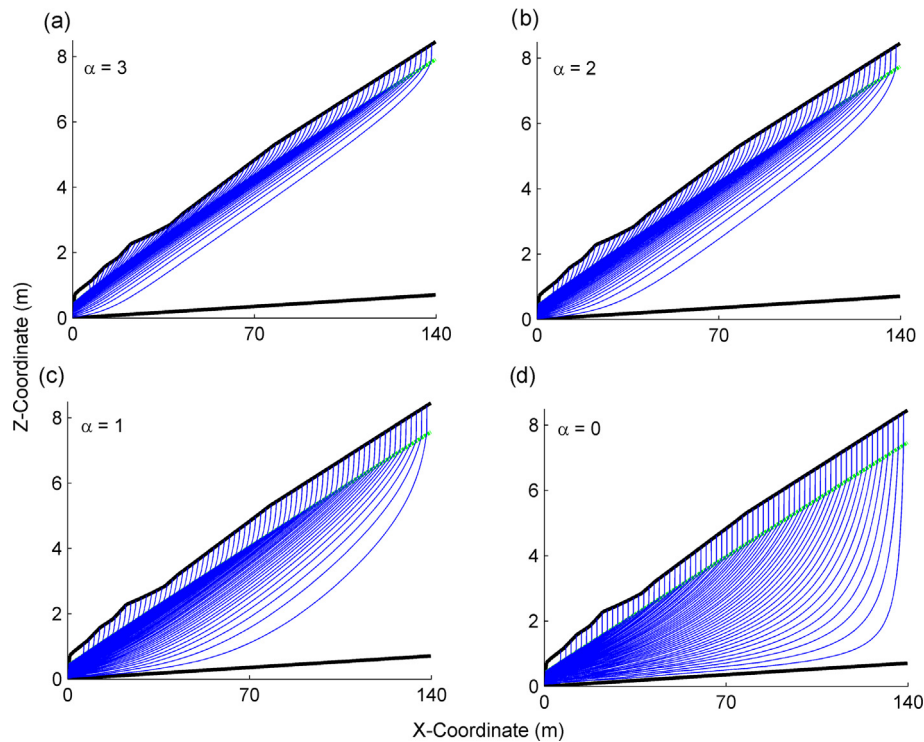
Fig. 3. Flow pathline distribution and water table (green line), for different rates in the exponential decline of k_s with soil depth (α). (a) $\alpha = 3$, (b) $\alpha = 2$, (c) $\alpha = 1$ and (d) $\alpha = 0$ (homogenous case). Only $\frac{1}{8}$ of all particles used in the RWPT analysis were shown. (For interpretation of the references to color in this figure legend, the reader is referred to the web version of this article.)
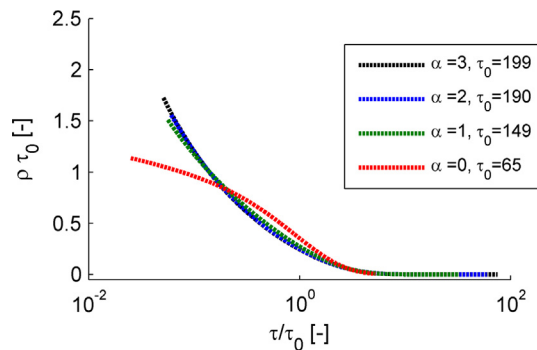

Fig. 4. Effect of rate of exponential decline in k_s with soil depth (α) on dimensionless TTD. τ_0 represents mean groundwater age (day). The Gamma shape parameter of the TTD varies from 0.92 to 0.50 as α increases.

The dimensionless transit time probability density function, $\rho \tau_0$, also suggests that as α increased the proportions of (relatively) early and late particle arrivals discharged into the stream increased markedly (Fig. 4), increasing the variability in transit times. This is associated with a considerable decrease in the Gamma shape parameter from 0.92 to 0.50 as α increased from 0 (homogenous case) to 3 (the extreme heterogeneous case). The mean groundwater age (τ_0) also increased, which can be tied to an overall decrease in k_s as α increased given an identical k_s along the topographic surface.

3.3. Effect of exponential decline in porosity with soil depth (η)

The effect of exponential decline in porosity with soil depth on TTD was assessed for two end members of α ($\alpha = 3$ and $\alpha = 0$). As η, the parameter describing the exponential decline in porosity with soil depth varied, flow pathline distribution did not differ (not

shown here). This was because the variation in porosity identically affected pore water velocity in both x and z directions in the entire domain (Eq. (3)). Changes in the strength of exponential decline in porosity with soil depth (η) impacted the dimensionless TTD and mean groundwater age; albeit this effect was more pronounced for homogenous K_s (Fig. 5b) compared to the case with an extreme vertical heterogeneity in K_s (Fig. 5a). As η increased, the variability of transit times relative to mean ground water age decreased for both K_s patterns. This was also supported by the increase in the Gamma shape parameters. Indeed, for the case with an extreme vertical heterogeneity in K_s with soil depth, as η increased, the higher and lower relative porosity at shallow and deep portions, respectively, canceled out higher and lower relative Darcy (Darcy–Buckingham) fluxes (Eq. (3)) at shallow and deep portions, which led to a small decrease in MTT and the variability of transit times. On the other hand, for the homogenous K_s, the pore water velocity of deeply penetrating pathlines increased considerably with an increase in η. This led to a pronounced decrease in MTT and the variability of transit times since these deep pathlines formed the tail of the TTD.

3.4. Effect of infiltration rate (R)

The model was used to assess the effect of infiltration rate on flow pathlines, groundwater table location, TTD and mean groundwater age. High flow (1.8 mm/d), average flow (0.8 mm/d), median flow (0.5 mm/d) and low flow (0.12 mm/d) during the study period were considered here as infiltration rates. As infiltration rate increased, shallow flow in the vicinity of the watercourse (the discharge area) also increased since the water table was raised to reach the superficial zone of higher conductivity closer to the topographic surface (Fig. 6). In addition, at the S-transect, it was observed that the infiltrating rainfall/snowmelt did not percolate deeper than 90 cm at S22 before and after spring flood based on
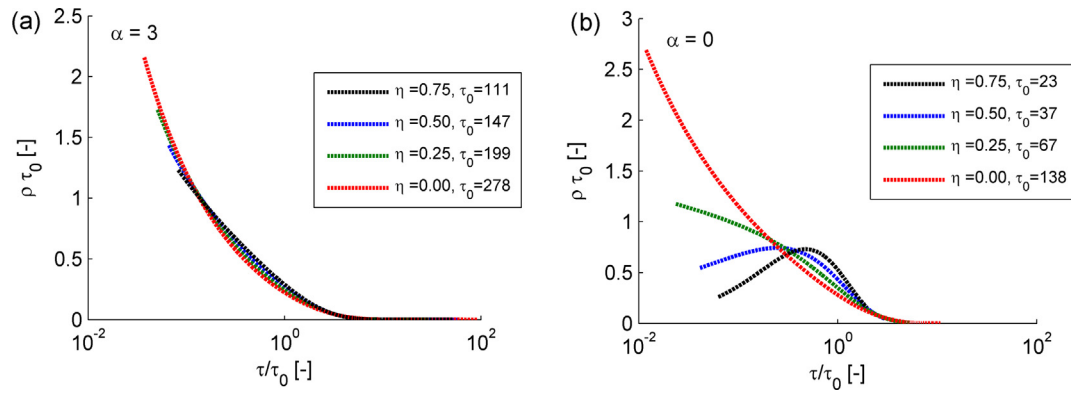
Fig. 5. Effect of the strength of exponential decline in porosity with depth (η) on the dimensionless transit time probability density function. τ_0 represents mean groundwater age (day). (a) $\alpha = 3$ (extreme vertical heterogeneity in K_s), the Gamma shape parameter varies from 0.43 to 0.66 as η increases from 0 to 0.75. (b) $\alpha = 0$ (homogenous K_s), the Gamma shape parameter varies from 0.63 to 1.70 as η increases from 0 to 0.75.
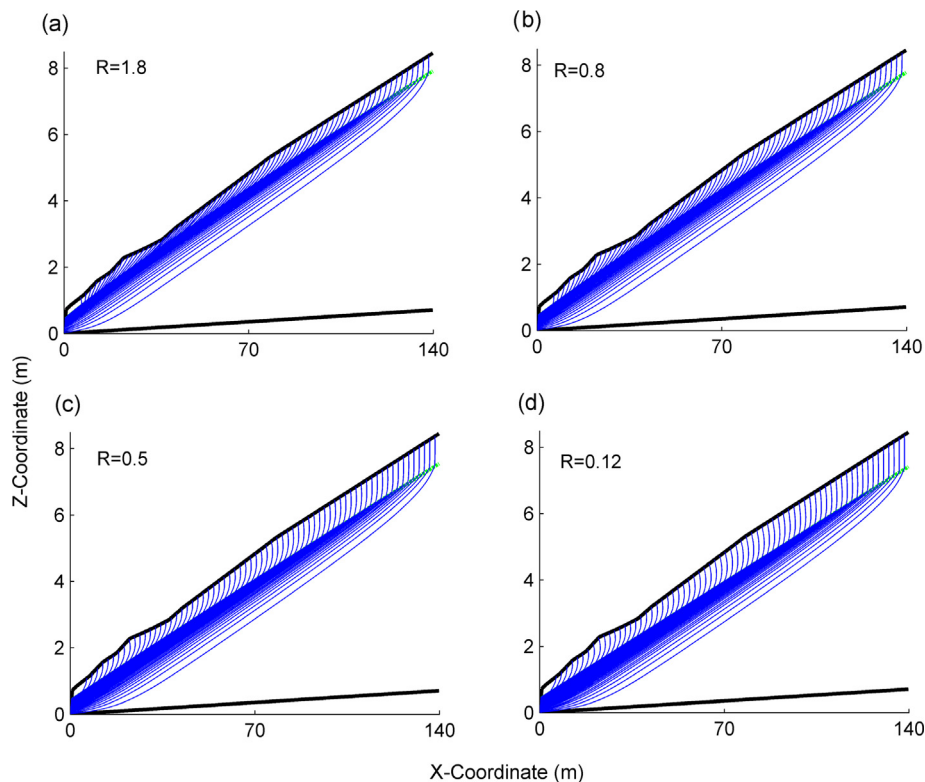

Fig. 6. Flow pathline distribution and water table (green line) for different values of infiltration rate (R). (a) $R = 1.8$ mm/d (high flow), (b) $R = 0.8$ mm/d (average flow), (c) $R = 0.5$ mm/d (median flow) and (d) $R = 0.12$ mm/d (low flow). Only $\frac{1}{8}$ of all particles used in the RWPT analysis were shown. (For interpretation of the references to color in this figure legend, the reader is referred to the web version of this article.)

the (δ^{18}O) analysis. This was comparable to the simulated flow pathlines with a flow pathline depth of almost 110–140 cm at S22 as infiltration rate decreased from high flow to low flow (Fig. 6).

There was an overall decrease in transit times of the water particles traversed between topographic surface and stream (Fig. 7a) as the infiltration rate increased. The MTT decreased almost exponentially (Fig. 7b). Fig. 7 shows that the longest transit time in response to the high flow rate (almost 10,000 days), was on the order of the MTT for low flow (6396 days). Infiltration rate, however, had a negligible impact on the shape of the dimensionless TTD, so the proportions of early and late particle arrivals discharged into the stream (relative to MTT). This held true regardless of the degree of vertical heterogeneity in K_s (Fig. 8). This was also

seen in the small variation in the Gamma shape parameter as infiltration rate varied from low flow to high flow. Indeed, although infiltration rate pronouncedly influenced the water table location and the transit time of water particles discharged into the surface water course, the impact on the "variability" of hillslope transit times relative to mean groundwater age was slight.

3.5. Effect of dispersivity (α_L and α_T)

Dispersivity is a characteristic property of the porous media, which represents the pore scale (micro) heterogeneity. The effect of different strengths of longitudinal and transverse dispersivity (α_L and α_T) on the dimensionless TTD and mean groundwater age for two end members of K_s vertical pattern was assessed. Four dif-
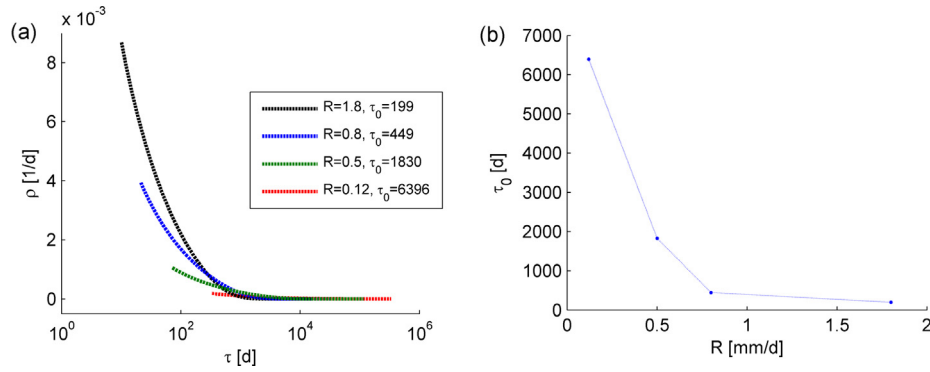
Fig. 7. Effect of infiltration rate (R [mm/d]) on transit times. (a) Transit time probability density function and (b) mean ground water age (τ_0).
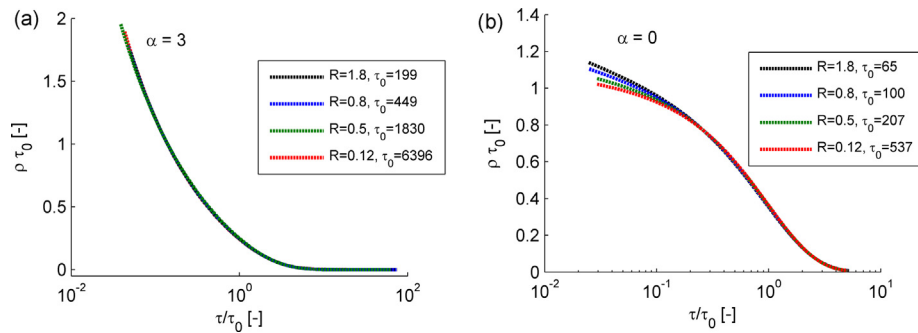

Fig. 8. Effect of infiltration rate (R [mm/d]) on dimensionless transit time distribution for two different rates of exponential decline in K_s with depth (α). (a) $\alpha = 3$ (extreme heterogeneity), the Gamma shape parameter varies from 0.52 to 0.50 as R increases from 0.12 to 1.8 mm/d. (b) $\alpha = 0$ (homogenous case), the Gamma shape parameter varies from 0.97 to 0.92 as R increases from 0.12 to 1.8 mm/d.
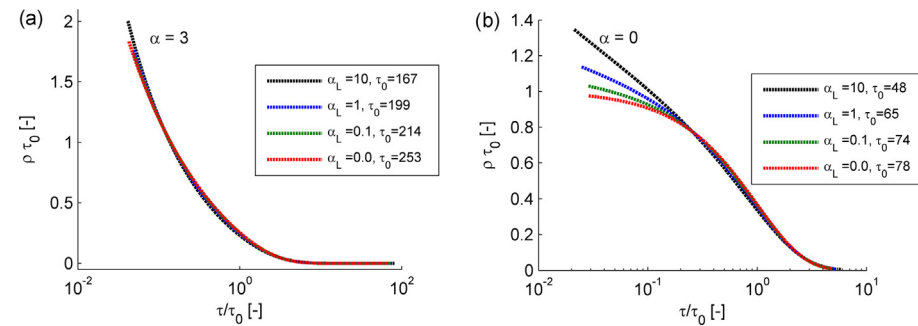

Fig. 9. Effect of longitudinal dispersivity (α_L [cm]) on dimensionless transit time probability density function for two different rates of exponential decline in K_s with soil depth (α). A transverse dispersivity (α_T) equals to $\frac{1}{100}$ of the longitudinal dispersivity was considered for each case. (a) $\alpha = 3$ (extreme heterogeneity in K_s), the Gamma shape parameter varies from 0.53 to 0.49 as α_L increases from 0 to 10 cm. (b) $\alpha = 0$ (homogenous K_s), the Gamma shape parameter varies from 1 to 0.85 as α_L increases from 0 to 10 cm.

ferent values of α_L equal to 10, 1, 0.1 and 0 cm were considered (Fig. 9). A transverse dispersivity (α_T) equal to $\frac{1}{100}$ of the longitudinal dispersivity was also considered for each case (Table 1). An increase in dispersivity decreased the MTT. However, the effect of dispersivity on the dimensionless TTD depended upon the degree of vertical heterogeneity in K_s. For homogenous K_s ($\alpha = 0$), an increase in dispersivity values slightly increased the proportions of young and old waters (relative to mean groundwater age). On the other hand, for extreme vertical heterogeneity in K_s ($\alpha = 3$), an increase in dispersivity had negligible effects on the variability of transit times. The influence of dispersivity on flow pathlines distribution throughout the hillslope was also negligible (not shown here).

3.6. Effect of hillslope length (L)

As hillslope length (i.e., the horizontal distance between surface water course and sub-catchment divide) increased, the variability of transit times changed only slightly at both end members of K_s vertical patterns (Fig. 10). This was reflected in the small decrease in the Gamma shape parameters. As hillslope length increased, the water table rose closer to the stream due to a larger amount of water that must traverse the same soil profile (not shown here). This led to a shallower unsaturated zone and a slightly increased proportion of young waters for both end members of K_s vertical patterns (Fig. 10). For the case with an extreme exponential vertical decline in K_s, the elevated water table further enhanced a
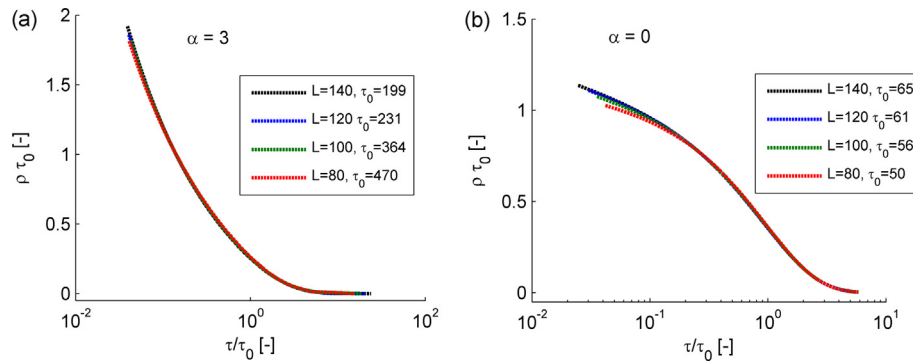
Fig. 10. Effect of hillslope length (L [m]) on the dimensionless transit time probability density function for two different rates of exponential decline in K_s with depth (α). (a) $\alpha = 3$ (extreme heterogeneity in K_s), the Gamma shape parameter varies from 0.55 to 0.50 as L increases from 80 m to 140 m. Even though Gamma shape parameter is almost insensitive to hillslope length, the MTT decreases significantly with an increase in hillslope length. (b) $\alpha = 0$ (homogenous K_s), the Gamma shape parameter varies from 0.95 to 0.92 as L increases from 80 m to 140 m. Again, Gamma shape parameter is almost insensitive to hillslope length, but the MTT increases slightly with an increase in hillslope length. For the particle tracking simulation in this analysis, particles initially located at each 25 cm interval along the topographic surface were used. Thus, the number of particles was not 560 for all examples, since the length of the hillslope varied.
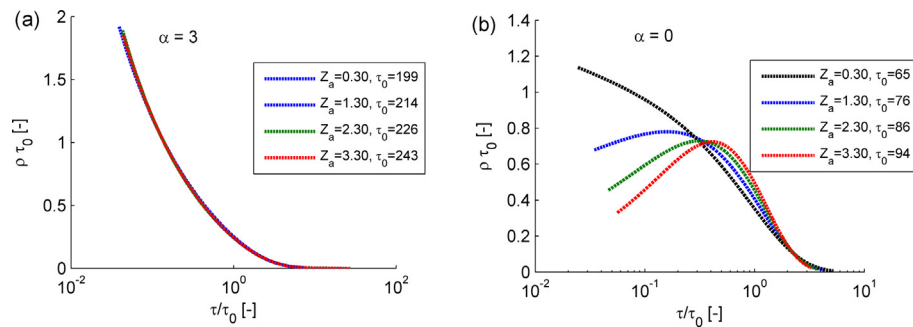

Fig. 11. Effect of the location of no-flow boundary underlying the hillslope on dimensionless transit time probability density function for two different rates of exponential decline in K_s with depth (α). (a) $\alpha = 3$ (extreme heterogeneity in K_s), the Gamma shape parameter varies from 0.50 to 0.48 as Z_a increases. (b) $\alpha = 0$ (homogenous K_s), the Gamma shape parameter varies from 0.92 to 1.52 as Z_a increases. While the gamma shape parameter changes little in the case of extreme K_s heterogeneity, the MTT increases by about 25% (from 199 to 243 days) across the explored range. On a relative scale, the MTT increases more in the case of homogeneous K_s, from 65 to 94 days (45%).

shallower flow circulation with a larger pore velocity in the more conductive portions of the aquifer closer to the topographic surface. Faster (and shallower) flow circulation together with smaller transit times in the unsaturated zone led to a considerable decrease in MTT as the hillslope length increased (Fig. 10a). On the other hand, for the homogenous K_s ($\alpha = 0$) with an almost uniform (with depth) pore water velocity in the entire saturated zone, the increase in the lengths of flow pathlines (as the hillslope length increased) was a dominant control on the slight increase in the MTT (Fig. 10b).

3.7. Effect of the location of the no-flow boundary underlying the hillslope (Z_a)

The original and alternative locations of the no-flow boundary underlying the hillslope for this assessment are shown in Fig. 1d (black and blue lines, respectively) with a minimum vertical distance of Z_a calculated between the stream bed and the no-flow boundary. Lowering the location of the no-flow boundary (i.e., increasing Z_a) had a negligible impact on the variability of transit times for the case with an extreme exponential vertical decline in K_s (Fig. 11a). This was because very few water particles penetrated the deeper portion of the aquifer. Indeed, the actual depth of the hydrologically active soil layer was almost constant (not varying with the location of the no-flow boundary at the bottom of the slope). The deeper parts of the hillslope acted as a low-flow or even no-flow zone for the case of an extreme exponential vertical decline in K_s. In the case of homogenous K_s, lowering the

no-flow boundary at depth promoted deeper flow pathlines and lessened the variability in transit times relative to MTT (Fig. 11b). In addition, MTT for both K_s vertical patterns increased when lowering the no-flow boundary at the bottom since it increased the extent of what the water particles could traverse and also slightly lowered the water table elevation (not shown here).

4. Discussion

The subsurface vertical permeability architecture and hydrological boundary locations affect the TTD and flow pathlines (Ali et al., 2014; Birkel et al., 2011; Hrachowitz et al., 2010; Kirchner et al., 2001). Few numerical experiments have investigated the impact of vertical decline in permeability on TTD either explicitly and implicitly (by using macro-dispersion) (Cardenas and Jiang, 2010; Kollet and Maxwell, 2008). However, these numerical experiments did not consider the interaction between vertical decline in permeability with the other subsurface controls such as location of hydrological boundaries and infiltration rate. More importantly, these approaches took into account only gradual vertical changes in the permeability pattern. Rapid changes in vertical heterogeneity in permeability is a characteristic feature of shallow till soils where k_s and porosity may decline abruptly (e.g., Grip, 2015; Lundin, 1982; Nyberg, 1995; Seibert et al., 2011). These tills are a common soil type in areas with a glaciation history. Recently, Ameli et al. (2016) introduced a new grid-free semi-analytical integrated flow and transport solution with an ability to explicitly and

exactly account for smooth to rapid exponential decline in k_s and porosity with soil depth. This, together with the ability to efficiently generate subsurface flow pathlines and transit times along the pathlines using continuous particle tracking, offers a framework to systematically assess how the rate of vertical decline in k_s and porosity interact with other hydrological controls (location of hillslope hydrological boundaries, dispersivity and infiltration rate) to influence the groundwater table location, flow pathline distribution, TTD and MTT.

The current study was designed to first determine the efficacy of this semi-analytical approach in simulating observed groundwater flow and transport dynamics along a well-studied, till-mantled hillslope on the Västrabäcken sub-catchment in Sweden. Our modeling results showed that the steady-state semi-analytical solution can accurately predict the observed groundwater depth for various flow rates within tens of meters from the stream, as well as the long-term TTD obtained from the convolution approach applied to the isotopic tracers. The simulated pathlines for the calibrated model were also consistent with the observation of little annual change in an isotopic hydrological tracer at 90 cm depth some 20 m from the stream on the hillslope.

The model was then used to examine systematically the influence of changing the (k_s) and porosity patterns with soil depth, mechanical dispersion, depth of the no-flow boundary underlying the hillslope, hillslope length and infiltration rate for computed MTT, TTD, and flow pathline distribution. Our results showed that an exponential decline in k_s with soil depth can significantly affect the flow pathlines and the variability (relative to MTT) of transit times. The results also showed that changes in porosity pattern can influence the shape of TTD and MTT, but these impacts are highly dependent upon the rate of K_s change with soil depth within the hillslope. While the impacts of systematic "macro scale" subsurface vertical heterogeneity (i.e., k_s and porosity changes with soil depth) on the structure of TTD was considerable, pore scale heterogeneity (represented in this paper by mechanical dispersivity) had only a slight impact on subsurface flow pathlines, TTD and MTT, particularly as the rate of vertical decline in K_s increased. This is consistent with the findings by Cardenas and Jiang (2010) and Fiori and Russo (2008).

Although both the infiltration rate and the pattern of vertical decline in K_s pronouncedly impact transit times, water table location, MTT and the shape of the regular (non-dimensionless) TTD, the infiltration rate has a negligible impact on the "variability" of transit times relative to MTT (and the shape of the dimensionless TTD). The results also suggest that the location of hydrological boundaries including water divide and no-flow boundary underlying the hillslope have negligible effects on the structure of dimensionless TTD and the variability of transit times as the rate of vertical decline in k_s increases. This may imply that accurate determination of the location of the no-flow boundary underlying the hillslope in subsurface flow and transport models is not necessary with regard to TTD delineation for the cases with extreme vertical exponential decline in K_s. This may become less true as the degree of vertical exponential decline in K_s decreases or other K_s-depth functions govern subsurface structure. For example, for the homogenous case, the location of hydrological boundaries has a larger effect on the TTD particularly the changes in the location of the no-flow boundary underlying the hillslope. A longer hillslope also increases the MTT for homogenous k_s but decreases the MTT for the extreme vertical decline in k_s.

Our model results obtained through virtual experiments are consistent with observations from experimental studies that showed that the shape parameter of Gamma distribution, which describes the variability of time-invariant transit times relative to MTT, had no relationship with precipitation intensity variations

but was closely related to catchment landscape organization (e.g., Hrachowitz et al., 2010). Indeed, this paper is the first modeling experiment that we are aware of that explicitly links the shape of the TTD and variability in transit times with subsurface vertical macro heterogeneity by considering a relatively rapid decline in Ks and porosity with soil depth as is common in till mantled catchments. The Gamma shape parameters reported in this paper also showed that as vertical heterogeneity in permeability increased, the behavior of the hillslope approached the fractal behavior. The conclusions made here can also provide a guideline for the required level of complexity in subsurface structure to explicitly and efficiently model flow pathlines and TTD.

While these results are interesting hydrologically, they may also open the door for greater insights into how systematic changes in runoff regimes related to climate and land use will influence hydrogeochemistry. Such changes in the MTT and TTD and the prevalence of specific flow paths can greatly impact reactive and non-reactive solute concentrations (e.g., Peters et al., 2014). Short term variation in flow pathlines have already been shown to be a first-order control on the concentration of dissolved organic carbon (Bishop et al., 2004) and landscape organization has been implicated in the more complex patterns of dissolved organic carbon (Troch et al., 2013) and nutrient processing (Pinay et al., 2015) in the stream network. With the insights from this current modeling study, and long-term predictions of the hydrological regime at a highly resolved spatial and temporal scale (Teutschbein et al., 2015), it should be possible to pose stronger hypotheses which can be tested using the decades of high-resolution data that are being developed at long term hydroecological research sites (like the Krycklan Catchment Study).

4.1. Need for future research

The semi-analytical solution used in this paper was a useful and appropriate tool for simulating flow and transport in a till environments as well as for systematically assessing the impact of vertical permeability architecture on time-invariant TTD and flow pathlines. However, the steady state condition is still a necessary assumption for most (semi)analytical solutions, including the one used in this paper. TTDs are by nature time variant (Harman, 2015; Klaus et al., 2015), and vary with precipitation regime (Sayama and McDonnell, 2009) as well as wetness conditions (Heidbüchel et al., 2013; Tetzlaff et al., 2014). While the time invariant TTD may still be valid for wet conditions with little seasonality and/or if one focuses on long term behavior of the catchment (see also Botter et al., 2010), most systems have time varying TTD. This can underestimate the proportion of early arrival waters in humid catchments (Botter, 2012; Hrachowitz et al., 2010). A time variant integrated subsurface flow and particle movement approach would be desirable for an explicit simulation of transient subsurface flow pathlines and transit times. This can be accomplished through application of robust numerical transient subsurface flow and transport solutions, or by adding a Laplace Transform simulator (in a manner similar to Bakker, 2013) to the present semi-analytical solution (something we plan to explore in the future). Notwithstanding, the steady-state assumption still seems to be valid for modeling flow pathlines and transit times in the riparian portion of the hillslope studied in this paper; although the validity of the steady state assumption weakens further away from the water course as one moves closer to the sub-catchment divide.

Another factor that should be examined in future work is the lateral variation in the pattern of k_s exponential decline. In this paper we ignored this feature and only considered vertical permeability patterns. The consistent underestimation of groundwater

depths at the water divide might be related in part to a different k_s profiles there compared to that closer to the stream where we had better data to parameterize the k_s depth profile. More importantly, the impact of large-scale variation in lateral permeability on TTD and flow pathlines may be significant and should be assessed systematically. This assessment can be accomplished in the future by the implementation of statistically driven large-scale lateral heterogeneity in the permeability.

Finally, topographic controls such as topographic convergences can also influence TTD and flow pathlines. A 2-D representation, as adopted in this study seems appropriate for the slope studied here since it was characterized by a fairly uniform geometry (width and slope). However, a study of other hillslopes with more variable geometries showed links between terrain convergence and flow paths in the riparian zone (Grabs et al., 2012). To apply the semi-analytical model to such cases one would thus have to overcome some of the limitations inherent in a 2-D hillslope representation. This could be achieved potentially by using 3-D semi-analytical model (e.g., Ameli and Craig, 2014), or a numerical subsurface flow and transport model, as well as by combining the semi-analytical model with mathematical approximations of hillslope geometries (Troch et al., 2002).

5. Conclusion

A semi-analytical series solution model was developed to simulate subsurface flow and particle movement in the well-studied S-transect hillslope on the Västrabäcken sub-catchment in Sweden. The steady state model emulated the observed groundwater depth–discharge relationship within tens of meters of the stream. The integrated model also reasonably simulated the hillslope TTD. The results also suggested that the macro scale vertical heterogeneity in subsurface permeability including exponential decline in saturated hydraulic conductivity and porosity with soil depth significantly impact the structure of TTD and the variability of transit times (relative to MTT) within the hillslope. The exponential decline in saturated hydraulic conductivity with depth also impacts the flow path distribution with shallower flow circulation as the strength of exponential decline in K_s increases. In contrast, subsurface pore scale micro heterogeneity (mechanical dispersion) only slightly influenced the variability of transit times and pathline distribution. The impact of infiltration rate was also negligible on the "variability" of transit times relative to MTT, while an increase in this rate significantly decreased the transit times and MTT in the hillslope. The location of the hydrological boundaries at the water divide and the no-flow boundary underlying the hillslope also influenced the TTD but only slightly when the rate of exponential vertical decline in K_s was large. Location of these boundaries had a somewhat larger effect in more homogeneous soils on the TTD. Our findings provide useful guidelines for understanding the required level of complexity in subsurface structure to explicitly model time invariant flow pathlines and TTD. Future work is needed to explicitly simulate "time variant" subsurface flow pathlines and transit time distributions on hillslopes with more complex topography where the soil properties can change with distance from the stream.

Acknowledgement

Appendix A. Semi-analytical subsurface flow solution

Ameli et al. (2016) have shown that the series solution to the saturated flow governing equation with no-flow conditions along the sides of the saturated domain and exponentially depth decaying saturated hydraulic conductivity with soil depth ($K_s = K_{s0}e^{\alpha(z-Z_t)}$) can be obtained in terms of discharge potential function ($\phi_s(x,z)$) as:

$$\phi_s(x,z) = A_0 + \sum_{n=1}^{N} \left(A_n \left[\cos\left(\frac{n\pi}{L}x\right)\exp(\gamma_n z) \right] + B_n \left[\cos\left(\frac{n\pi}{L}x\right)\exp(\bar{\gamma}_n z) \right] \right)$$

(A.1)

$$\gamma_n = \frac{-\alpha}{2} + \frac{1}{2}\sqrt{\alpha^2 + \left(\frac{2n\pi}{L}\right)^2}, \quad \bar{\gamma}_n = \frac{-\alpha}{2} - \frac{1}{2}\sqrt{\alpha^2 + \left(\frac{2n\pi}{L}\right)^2}$$

where $\phi_s(x,z) = K_{s0}h_s(x,z)$.

The series solution for the unsaturated moisture movement with exponentially depth decaying saturated hydraulic conductivity with soil depth can be calculated in terms of Kirchhoff potential (ϕ_u) as:

$$\phi_u(x,z) = C_0[\exp(-\beta z)] - \sum_{m=1}^{M} \left(C_m \left[\cos\left(\frac{m\pi}{L}x\right)\exp(\pounds_m z) \right]\frac{\pounds_m}{\frac{m\pi}{L}} \right.$$
$$\left. + D_m \left[\cos\left(\frac{m\pi}{L}x\right)\exp(\bar{\pounds}_m z) \right]\frac{\bar{\pounds}_m}{\frac{m\pi}{L}} \right)$$

(A.2)

$$\pounds_m = \frac{-(\alpha+\beta)}{2} + \frac{1}{2}\sqrt{(\alpha+\beta)^2 - 4\alpha\beta + \left(\frac{2n\pi}{L}\right)^2}, \bar{\pounds}_m$$
$$= \frac{-(\alpha+\beta)}{2} - \frac{1}{2}\sqrt{(\alpha+\beta)^2 - 4\alpha\beta + \left(\frac{2n\pi}{L}\right)^2}$$

where $\phi_u(\varphi) = \frac{K_{s0}\exp(\beta(\varphi-\varphi^e))}{\beta}$.

In the above equations h_s [L] is the total hydraulic head, φ is suction pressure head [L], L is aquifer length, K_{s0} [L T^{-1}] is the saturated hydraulic conductivity along the topographic surface $Z_t(x)$, α is the parameter of the exponential relationship between saturated hydraulic conductivity with soil depth, β and φ^e are the sorptive number and air entry pressure of the Gardner's constitutive function (Gardner, 1958) used to characterize the suction-hydraulic conductivity relationship in the vadose zone. In Eqs. (A.1) and (A.2), additionally, n and m denote the coefficient index, and A_n, B_n, C_m, D_m are the unknown series coefficients associated with the nth and mth coefficient index, respectively. N and M also refer to the total number of terms in the series solutions to the saturated and unsaturated flow governing equations, respectively. The unknown series solution coefficients (A_n, B_n and C_m, D_m) for Eqs. (A.1) and (A.2) were calculated by enforcing the boundary conditions at the top and the bottom of saturated and unsaturated zones. These boundary conditions were imposed using a simple least square scheme at control points located along each interface. These boundary conditions include Neumann boundary conditions (infiltration rate) along the top of the unsaturated domain (i.e. land surface), constant head (air entry pressure) along the unsaturated domain bottom (i.e. the *a priori* unknown top of the capillary fringe zone interface), continuity of flux between saturated and unsaturated zones along the top of the saturated domain (again the *a priori* unknown top of the capillary fringe zone interface), no-flow condition along the bottom boundary of the computational domain and constant head at the stream. The *a priori* unknown location of top of capillary fringe was also obtained using an iterative scheme between the saturated and unsaturated solutions. The water table location ($Z_{wt}(x)$ in Fig. 1d) was then calculated as the boundary with a zero pressure head. We refer the readers Ameli et al.

(2016) for a detailed discussion of the mathematical formulation of series solution method, boundary conditions, least square scheme used to enforce boundary conditions and iterative algorithm used to determine the *a priori* unknown location of water table.

References

Ali, M., Fiori, A., Russo, D., 2014. A comparison of travel-time based catchment transport models, with application to numerical experiments. J. Hydrol. 511, 605–618.

Ameli, A.A., Craig, J.R., 2014. Semianalytical series solutions for three-dimensional groundwater-surface water interaction. Water Resour. Res. 50 (5).

Ameli, A.A., Craig, J.R., Wong, S., 2013. Series solutions for saturated–unsaturated flow in multi-layer unconfined aquifers. Adv. Water Resour. 60, 24–33.

Ameli, A.A., McDonnell, J.J., Bishop, K., 2016. The exponential decline in saturated hydraulic conductivity with depth and its effect on water flow paths and transit time distribution. Hydrol. Process. http://dx.doi.org/10.1002/hyp.10777.

Bakker, M., 2013. Semi-analytic modeling of transient multi-layer flow with TTim. Hydrogeol. J. 21 (4), 935–943. http://dx.doi.org/10.1007/s10040-013-0975-2.

Basu, N.B., Jindal, P., Schilling, K.E., Wolter, C.F., Takle, E.S., 2012. Evaluation of analytical and numerical approaches for the estimation of groundwater travel time distribution. J. Hydrol. 475, 65–73.

Birkel, C., Tetzlaff, D., Dunn, S.M., Soulsby, C., 2011. Using lumped conceptual rainfall–runoff models to simulate daily isotope variability with fractionation in a nested mesoscale catchment. Adv. Water Resour. 34 (3), 383–394.

Bishop, K., Lee, Y.-H., Pettersson, C., Allard, B., 1995. Terrestrial sources of methylmercury in surface waters: the importance of the riparian zone on the Svartberget catchment. Water Air Soil Pollut. 80 (1–4), 435–444.

Bishop, K., Seibert, J., Köhler, S., Laudon, H., 2004. Resolving the double paradox of rapidly mobilized old water with highly variable responses in runoff chemistry. Hydrol. Process. 18 (1), 185–189. http://dx.doi.org/10.1002/hyp.5209.

Bishop, K.H., 1991. Episodic Increases in Stream Acidity, Catchment Flow Pathways and Hydrograph Separation. University of Cambridge.

Botter, G., 2012. Catchment mixing processes and travel time distributions. Water Resour. Res. 48 (5).

Botter, G., Bertuzzo, E., Rinaldo, A., 2010. Transport in the hydrologic response: travel time distributions, soil moisture dynamics, and the old water paradox. Water Resour. Res. 46 (3).

Botter, G., Bertuzzo, E., Rinaldo, A., 2011. Catchment residence and travel time distributions: the master equation. Geophys. Res. Lett. 38 (11).

Cardenas, M.B., Jiang, X.-W., 2010. Groundwater flow, transport, and residence times through topography-driven basins with exponentially decreasing permeability and porosity. Water Resour. Res. 46 (11).

Cory, N., Laudon, H., Köhler, S., Seibert, J., Bishop, K., 2007. Evolution of soil solution aluminum during transport along a forested boreal hillslope. J. Geophys. Res.: Biogeosci. (2005–2012) 112 (G3).

Eklöf, K. et al., 2014. Impact of forestry on total and methyl-mercury in surface waters: distinguishing effects of logging and site preparation. Environ. Sci. Technol. 48 (9), 4690–4698.

Fiori, A., Russo, D., 2008. Travel time distribution in a hillslope: insight from numerical simulations. Water Resour. Res. 44 (12).

Fiori, A., Russo, D., Di Lazzaro, M., 2009. Stochastic analysis of transport in hillslopes: travel time distribution and source zone dispersion. Water Resour. Res. 45 (8).

Gardner, W., 1958. Some steady-state solutions of the unsaturated moisture flow equation with application to evaporation from a water table. Soil Sci. 85 (4), 228–232.

Godsey, S.E. et al., 2010. Generality of fractal 1/f scaling in catchment tracer time series, and its implications for catchment travel time distributions. Hydrol. Process. 24 (12), 1660–1671.

Goode, D.J., 1996. Direct simulation of groundwater age. Water Resour. Res. 32 (2), 289–296.

Grabs, T., Bishop, K., Laudon, H., Lyon, S.W., Seibert, J., 2012. Riparian zone hydrology and soil water total organic carbon (TOC): implications for spatial variability and upscaling of lateral riparian TOC exports. Biogeosciences 9 (10), 3901–3916.

Grip, H., 2015. Sweden's first forest hydrology field study 1905–1926: contemporary relevance of inherited conclusions and data from the Rokliden Hillslope. Hydrol. Process 29 (16).

Harman, C.J., 2015. Time-variable transit time distributions and transport: theory and application to storage-dependent transport of chloride in a watershed. Water Resour. Res. 51 (1), 1–30.

Harr, R.D., 1977. Water flux in soil and subsoil on a steep forested slope. J. Hydrol. 33 (1), 37–58.

Heidbüchel, I., Troch, P.A., Lyon, S.W., 2013. Separating physical and meteorological controls of variable transit times in zero-order catchments. Water Resour. Res. 49 (11), 7644–7657.

Hrachowitz, M. et al., 2009. Using long-term data sets to understand transit times in contrasting headwater catchments. J. Hydrol. 367 (3), 237–248.

Hrachowitz, M., Soulsby, C., Tetzlaff, D., Malcolm, I., Schoups, G., 2010. Gamma distribution models for transit time estimation in catchments: physical interpretation of parameters and implications for time-variant transit time assessment. Water Resour. Res. 46 (10).

Kirchner, J.W., Feng, X., Neal, C., 2000. Fractal stream chemistry and its implications for contaminant transport in catchments. Nature 403 (6769), 524–527.

Kirchner, J.W., Feng, X., Neal, C., 2001. Catchment-scale advection and dispersion as a mechanism for fractal scaling in stream tracer concentrations. J. Hydrol. 254 (1), 82–101.

Kirchner, J., 2016. Aggregation in environmental systems–Part 1: Seasonal tracer cycles quantify young water fractions, but not mean transit times, in spatially heterogeneous catchments. Hydrol. Earth Syst. Sci 20, 279–297.

Klaminder, J. et al., 2006. Flux rates of atmospheric lead pollution within soils of a small catchment in northern Sweden and their implications for future stream water quality. Environ. Sci. Technol. 40 (15), 4639–4645.

Klaus, J., Chun, K.P., McGuire, K.J., McDonnell, J.J., 2015. Temporal dynamics of catchment transit times from stable isotope data. Water Resour. Res. 51 (6).

Kollet, S.J., Maxwell, R.M., 2008. Demonstrating fractal scaling of baseflow residence time distributions using a fully-coupled groundwater and land surface model. Geophys. Res. Lett. 35 (7).

Laudon, H., Seibert, J., Köhler, S., Bishop, K., 2004. Hydrological flow paths during snowmelt: congruence between hydrometric measurements and oxygen 18 in meltwater, soil water, and runoff. Water Resour. Res. 40 (3).

Laudon, H. et al., 2013. The Krycklan Catchment Study—a flagship infrastructure for hydrology, biogeochemistry, and climate research in the boreal landscape. Water Resour. Res. 49 (10), 7154–7158.

Leith, F. et al., 2014. Carbon dioxide transport across the hillslope-riparian-stream continuum in a boreal headwater catchment. Biogeosci. Discuss. 11 (11), 15585–15619.

Lundin, L., 1982. Soil moisture and ground water in till soil and the significance of soil type for runoff.—UNGI Rapport Nr 56, Uppsala, 216 pp. Swedish, English summary.

Maxwell, R.M. et al., 2015. The imprint of climate and geology on the residence times of groundwater. Geophys. Res. Lett 43 (2).

McDonnell, J.J., Beven, K., 2014. Debates—the future of hydrological sciences: a (common) path forward? A call to action aimed at understanding velocities, celerities and residence time distributions of the headwater hydrograph. Water Resour. Res. 50 (6), 5342–5350.

McGuire, K.J., McDonnell, J.J., 2010. Hydrological connectivity of hillslopes and streams: characteristic time scales and nonlinearities. Water Resour. Res. 46 (10). http://dx.doi.org/10.1029/2010wr009341.

Molénat, J., Gascuel-Odoux, C., Aquilina, L., Ruiz, L., 2013. Use of gaseous tracers (CFCs and SF 6) and transit-time distribution spectrum to validate a shallow groundwater transport model. J. Hydrol. 480, 1–9.

Nyberg, L., 1995. Water flow path interactions with soil hydraulic properties in till soil at Gårdsjön, Sweden. J. Hydrol. 170 (1), 255–275.

Nyberg, L., Stähli, M., Mellander, P.E., Bishop, K.H., 2001. Soil frost effects on soil water and runoff dynamics along a boreal forest transect: 1. Field investigations. Hydrol. Process. 15 (6), 909–926.

Peralta-Tapia, A. et al., 2016. Hydroclimatic influences on non-stationary transit time distributions in a boreal headwater catchment. J. Hydrol. 543 (PA), 7–16.

Peralta-Tapia, A., Sponseller, R., Tetzlaff, D., Soulsby, C., Laudon, H., 2014. Connecting precipitation inputs and soil flow pathways to stream water in contrasting boreal catchments. Hydrol. Process. 29 (16).

Peters, N.E., Burns, D.A., Aulenbach, B.T., 2014. Evaluation of high-frequency mean streamwater transit-time estimates using groundwater age and dissolved silica concentrations in a small forested watershed. Aquat. Geochem. 20 (2–3), 183–202.

Pinay, G. et al., 2015. Upscaling nitrogen removal capacity from local hotspots to low stream orders' drainage basins. Ecosystems, 1–20.

Rinaldo, A. et al., 2015. Storage selection functions: a coherent framework for quantifying how catchments store and release water and solutes. Water Resour. Res. 51 (6), 4840–4847.

Rinaldo, A. et al., 2011. Catchment travel time distributions and water flow in soils. Water Resour. Res. 47 (7).

Salamon, P., Fernàndez-Garcia, D., Gómez-Hernández, J.J., 2006. A review and numerical assessment of the random walk particle tracking method. J. Contam. Hydrol. 87 (3), 277–305.

Sayama, T., McDonnell, J.J., 2009. A new time-space accounting scheme to predict stream water residence time and hydrograph source components at the watershed scale. Water Resour. Res. 45 (7).

Seibert, J., 2000. Multi-criteria calibration of a conceptual runoff model using a genetic algorithm. Hydrol. Earth Syst. Sci. Discuss. 4 (2), 215–224.

Seibert, J., Bishop, K., Nyberg, L., Rodhe, A., 2011. Water storage in a till catchment. I: Distributed modelling and relationship to runoff. Hydrol. Process. 25 (25), 3937–3949.

Seibert, J., Bishop, K., Rodhe, A., McDonnell, J.J., 2003. Groundwater dynamics along a hillslope: a test of the steady state hypothesis. Water Resour. Res. 39 (1). http://dx.doi.org/10.1029/2002wr001404.

Seibert, J. et al., 2009. Linking soil-and stream-water chemistry based on a Riparian flow-concentration integration model. Hydrol. Earth Syst. Sci. 13 (12), 2287–2297.

Stähli, M., Nyberg, L., Mellander, P.E., Jansson, P.E., Bishop, K.H., 2001. Soil frost effects on soil water and runoff dynamics along a boreal transect: 2. Simulations. Hydrol. Process. 15 (6), 927–941.

Tetzlaff, D., Birkel, C., Dick, J., Geris, J., Soulsby, C., 2014. Storage dynamics in hydropedological units control hillslope connectivity, runoff generation, and the evolution of catchment transit time distributions. Water Resour. Res. 50 (2), 969–985.

Teutschbein, C., Grabs, T., Karlsen, R., Laudon, H., Bishop, K., 2015. Hydrological response to changing climate conditions: spatial streamflow variability in the boreal region. Water Resour. Res. 51 (12), 9425–9446.

Troch, P., Van Loon, E., Hilberts, A., 2002. Analytical solutions to a hillslope-storage kinematic wave equation for subsurface flow. Adv. Water Resour. 25 (6), 637–649.

Troch, P.A. et al., 2013. The importance of hydraulic groundwater theory in catchment hydrology: the legacy of Wilfried Brutsaert and Jean-Yves Parlange. Water Resour. Res. 49 (9), 5099–5116.

Vaché, K.B., McDonnell, J.J., 2006. A process-based rejectionist framework for evaluating catchment runoff model structure. Water Resour. Res. 42 (2).

Weiler, M., McDonnell, J., 2004. Virtual experiments: a new approach for improving process conceptualization in hillslope hydrology. J. Hydrol. 285 (1–4), 3–18. http://dx.doi.org/10.1016/s0022-1694(03)00271-3.

Woolfenden, L.R., Ginn, T.R., 2009. Modeled ground water age distributions. Groundwater 47 (4), 547–557.